Research Square

Preprints are preliminary reports that have not undergone peer review.
They should not be considered conclusive, used to inform clinical practice,
or referenced by the media as validated information.

Perovskite superlattices with efficient carrier dynamics

Sheng Xu (shengxu@ucsd.edu)
University of California, San Diego https://orcid.org/0000-0002-3120-4992
Yusheng Lei
University of Californian San Diego
Yuheng Li
University of California San Diego https://orcid.org/0000-0002-1865-1122
Chengchangfeng Lu
University of California San Diego
Qizhang Yan
University of California San Diego https://orcid.org/0000-0002-3798-642X
Huaxin Gong
Stanford University
Song Zhang
Stanford University
Jiayun Zhou
University of California, San Diego
Ruiqi Zhang
University of California San Diego
Yimu Chen
University of California, San Diego
Hsinhan Tsai
Los Alamos National Lab https://orcid.org/0000-0002-1492-1279
Yue Gu
UC San Diego https://orcid.org/0000-0003-0437-5339
Hongjie Hu
University of California, San Diego
Yu-Hwa Lo
University of California, San Diego https://orcid.org/0000-0003-4602-1627
Wanyi Nie
Los Alamos National Laboratory https://orcid.org/0000-0002-5909-3155
Taeyoon Lee
Yonsei University https://orcid.org/0000-0002-8269-0257
Jian Luo

University of California, San Diego

Kesong Yang

University of California San Diego,

Kyung-In Jang

Daegu Gyeongbuk Institute of Science and Technology

Physical Sciences - Article

Keywords: low-dimensional metal halide perovskites, carrier transport, organic spacers

Posted Date: November 12th, 2021

DOI: https://doi.org/10.21203/rs.3.rs-1048977/v1

License: This work is licensed under a Creative Commons Attribution 4.0 International License.
Read Full License

Version of Record: A version of this preprint was published at Nature on August 10th, 2022. See the published version at https://doi.org/10.1038/s41586-022-04961-1.

Perovskite superlattices with efficient carrier dynamics

Yusheng Lei[1,2*], Yuheng Li[1*], Chengchangfeng Lu[3], Qizhang Yan[1], Huaxin Gong[2], Song Zhang[2], Jiayun Zhou[4], Ruiqi Zhang[1], Yimu Chen[1], Hsinhan Tsai[5], Yue Gu[4], Hongjie Hu[1], Yu-Hwa Lo[3], Wanyi Nie[5], Taeyoon Lee[6,7], Jian Luo[1,4], Kesong Yang[1], Kyung-In Jang[8], Sheng Xu[1,4,5,9#].

[1]Department of Nanoengineering, University of California San Diego, La Jolla, CA 92093-0448, USA
[2]Department of Chemical Engineering, Stanford University, Stanford, CA 94305, USA
[3]Department of Electrical and Computer Engineering, University of California San Diego, La Jolla, CA 92093, USA
[4]Material Science and Engineering Program, University of California San Diego, La Jolla, CA 92093-0418, USA
[5]Los Alamos National Laboratory, Los Alamos, NM 87545, USA
[6]School of Electrical and Electronic Engineering, Yonsei University, Seoul 03722, Republic of Korea.
[7]Department of Bio and Brain Engineering, Korea Institute of Science and Technology, Republic of Korea.
[8]Department of Robotics Engineering, Daegu Gyeongbuk Institute of Science and Technology, Daegu 42988, Republic of Korea.
[9]Department of Bioengineering, University of California San Diego, La Jolla, CA 92093-0412, USA
[*]These authors contributed equally to this work.
[#]Email: shengxu@ucsd.edu

Abstract

Compared with their three-dimensional counterparts, low-dimensional metal halide perovskites with periodic inorganic/organic structures have shown promising stability and hysteresis-free electrical performance, which paves the way for next-generation optoelectronic devices. However, when integrated in devices, they have relatively limited efficiencies because devices usually require carrier transport through the film thickness direction. In conventionally grown single crystals, the carrier transport in the thickness direction is hindered by the insulating organic spacers. In addition, the strong quantum confinement from the organic spacers limits the generation and transport of free carriers. The carrier dynamics is further compromised by the presence of grain boundaries in polycrystals. Here, we report a low-dimensional metal halide perovskite superlattice with efficient carrier transport in three dimensions by epitaxial growth. Epitaxy on a slightly lattice-mismatched substrate compresses the organic spacers in the superlattice, which weakens the quantum confinement and further improves carrier dynamics. The performance of a low-dimensional perovskite superlattice solar cell has been certified under the quasi-steady state for the first time. Moreover, the device shows an unusually high open-circuit voltage, due to a unique intra-band exciton relaxation mechanism.

Metal halide perovskites, with a general formula of AMX_3 (e.g., A = $CH_3NH_3^+$ (MA), $HC(NH_2)_2^+$, Cs^+, Rb^+; M = Pb^{2+}, Sn^{2+}; X = Cl^-, Br^-, I^-), are emerging as next-generation optoelectronic materials because of their phenomenal performance and processability in low-cost solutions[1-3]. However, their practical applications have been hindered by three issues: instability[4], electrical hysteresis[5], and toxicity[6]. Recently, low-dimensional (two-dimensional (2D) and quasi-2D) metal halide perovskites with a formula of $B_2A_{n-1}M_nX_{3n+1}$ (e.g., B = R-NH_3^+) have been invented to mediate the instability and hysteresis issues[7-11]. In these materials, the insulating ammonium interlayer spacers divide the semiconductive metal-halide structure into slabs, forming a multiple-quantum-well[12-15]. Existing single crystals are grown with the insulating organic spacers parallel to the substrate surface and cannot support carrier transport in the film thickness direction, which is required for device integration[16]. Moreover, the strong confinement of the multiple-quantum-well leads to a large exciton binding energy, which limits the generation and transport of carriers within the inorganic slabs[16,17]. Polycrystals contain grain boundaries that further compromise carrier dynamics[18]. Furthermore, lead-free metal halide perovskites have been developed, but their device performance is limited by their low crystallinity and structural instability[19].

Here, we report a $BA_2MA_{n-1}Sn_nI_{3n+1}$ (BA: butylammonium; n = 1, 3, 5) superlattice with long-range order. The superlattice was epitaxially grown on a 3D perovskite substrate. The inorganic slabs are aligned vertical to the substrate and interconnected in a crisscross 2D network parallel to the substrate, leading to efficient carrier transport both in-plane and out-of-plane. In addition,

due to the lattice mismatch with the substrate, the superlattice is under compressive strain, which reduces the width of the organic spacers. This weakens the quantum confinement of the organic spacers and thus further improves the carrier dynamics of the superlattice. The performance of a Bi^{3+} alloyed superlattice solar cell has been certified under the quasi-steady state for the first time, with a stable 12.36% photoelectric conversion efficiency and an unusually high open-circuit voltage.

We studied the growth process and structure of BA_2SnI_4 (n = 1) superlattice on a $MAPb_{0.5}Sn_{0.5}Br_3$ substrate. The superlattice is formed by a unique epitaxial mechanism (Supplementary Discussion 1). The Sn-I slabs exhibit a favorable epitaxial relationship with the substrate but cannot form a horizontally aligned lattice[20-22], which would contain thermodynamic unstable high n value structures (Supplementary Fig. 1)[15]. A vertically aligned lattice structure is energetically most favorable under experimental conditions in this work. Scanning electron microscopy images reveal that the crystals first grow into crisscross vertical thin plates (Fig. 1a; Supplementary Fig. 2). This is because the crystal structure of the substrate is cubic, and therefore the epitaxial growth behavior along the a and b directions is symmetric. As the growth progresses, they merge into a smooth film (Fig. 1a; Supplementary Fig. 2). Similar growth behavior is observed in other low-dimensional perovskites grown on different 3D perovskite substrates (Supplementary Fig. 3). Cryogenic-scanning transmission electron microscope was used to study the structure of a single plate, which exhibits an anisotropic structure (Fig. 1b). The a-c plane image shows a periodic distribution of inorganic Sn-I slabs

and organic BA spacers along the *a* direction (Fig. 1b, middle; Supplementary Fig. 4)[23]. The *b*-*c* plane image shows a continuous Sn-I slab with a coherent heteroepitaxial interface with the substrate (Fig. 1b, right). Therefore, the crisscross vertical plates on the substrates create a 3D network of Sn-I slabs, unseen in any polycrystals (Supplementary Fig. 5) or conventionally grown single crystals[7,12].

To further study the crystal orientation in the *a*-*b* plane, we measured polarization-dependent photocurrent of the superlattice and a conventionally grown single crystal with a linearly polarized excitation source (Fig. 1c). The results in both show a strong dependence on the polarization direction, but the response of the superlattice has a 90° period while that of the conventionally grown single crystal has a 180° period. This is because the inorganic slabs are aligned in two perpendicular orientations in the *a*-*b* plane of the superlattice, but in only one orientation of the conventionally grown single crystal (Supplementary Fig. 6). Similar trends can also be observed in the carrier lifetime obtained from orientation-dependent transient photovoltage measurements (Fig. 1d; Supplementary Fig. 7). These results collectively support that the superlattice has Sn-I slabs interconnected, with numerous crisscross thin plates merged in the *a*-*b* plane.

Because of the interconnected Sn-I slabs, carriers in the superlattice does not need to cross any grain boundaries or organic spacers. This allows the superlattice to have more efficient carrier dynamics along the film thickness (*c*) direction compared to its polycrystalline and

conventionally grown single crystal counterparts. Transient photocurrent measurements along the film thickness direction show a much higher carrier mobility in the superlattice than in the polycrystalline or conventionally grown single crystal sample (Fig. 2a). The grain boundaries in the polycrystal act as traps, which significantly reduce carrier mobility (Supplementary Fig. 8)[22]. The conventionally grown single crystal shows the lowest mobility, with only in-plane carrier transport (Supplementary Fig. 9). Power-dependent time-resolved photoluminescence measurements reveal that the superlattice has a longer carrier lifetime than the polycrystal (Fig. 2b), indicating minimal restriction of the carriers in the superlattice. Additionally, the superlattice shows better tolerance to high excitation power than the polycrystal, suggesting that better crystallinity can reduce material degradation under high excitation power[24].

The structural advantages of the superlattice are validated with temperature-dependent photovoltaic *J-V* characteristics of a BA_2SnI_4 solar cell. Solar cell fabrication was conducted on the as-grown film to minimize any possible confounding factors introduced by the fabrication process (Supplementary Fig. 10)[22]. As the temperature gradually drops, thermal energy becomes too small for the carriers to overcome barriers (e.g., due to ionized impurity scattering), so the fill factor (*F.F.*) decreases substantially for both the superlattice and polycrystalline devices (Fig. 2c). However, the decrease is less significant in the superlattice, indicating lower internal energy barriers and a higher charge-collection efficiency[25].

We measured the electron-beam-induced-current to directly visualize carrier transport

behaviors. For the polycrystal, the collected currents on the thin film surface heavily depend on the grain orientations, indicating the existence of strong barriers for carrier transport (Fig. 2d, left). In contrast, the superlattice yields higher and much more uniform currents due to the well-aligned crystal structure (Fig. 2d, right). Note that the superlattice currents exhibit a crisscross pattern due to the imperfect merging of the crystals during solution growth (Supplementary Fig. 11). Similar observations can also be made in the sample cross-sections (Fig. 2e; Supplementary Discussion 2).

The improved carrier dynamics of the superlattice allow a higher absorber thickness and thus more efficient light harvesting. The absorber thickness of the polycrystalline devices is usually highly restricted because of the limited carrier diffusion length[25]. For polycrystalline BA_2SnI_4, the external quantum efficiency (EQE) peaks at an absorber thickness of ~400 nm (Fig. 2f, top). Due to the improved carrier dynamics in the superlattice, the absorber thickness can be increased to ~700 nm with enhanced light absorption and thus EQE (Fig. 2f, bottom).

We investigated the heteroepitaxial strain in the BA_2SnI_4 superlattice quantitatively by X-ray diffraction. Compared to conventionally grown single crystals, high overall compressive strains are present in the superlattice along the *a* and *b* directions, at ~8.59% and ~1.32%, respectively (Fig. 3a, top); a tensile strain of ~0.99% is present in the *c* direction due to Poisson effect (Fig. 3a, bottom; Supplementary Discussion 3, Supplementary Table 1)[26]. These strains are validated by calculations using the lattice constants extracted from the scanning

transmission electron microscope images (Supplementary Fig. 4, Supplementary Discussion 3). Structural computation by density-functional theory (DFT) further reveals that the lattice constant of Sn-I slabs in the *a* direction is compressed from ~6.04 Å to ~5.94 Å (Supplementary Fig. 12), yielding a ~1.66% strain, which is close to the 1.32% strain in the *b* direction; the width of the organic spacer is compressed from ~7.00 Å to ~5.98 Å (Supplementary Figs. 12 and 13), corresponding to a 14.6% strain. Therefore, the high compressive strain is mostly accommodated by the organic spacer. High strain reduces the stability of the superlattice (Supplementary Figs. 14 and 15). For general heteroepitaxial $BA_2MA_{n-1}Sn_nI_{3n+1}$, as *n* increases, the volume ratio of the Sn-I slabs increases, and the overall lattice strain decreases (Fig. 3b), and the structure is more stable. Moreover, lower strain results in less structural defects and smoother surfaces (Fig. 3b, inset images).

To avoid potential phase change and achieve reliable measurements of the superlattice, we chose $BA_2MA_2Sn_3I_{10}$ (n = 3) to study their strain-controlled optoelectronic properties, and found that the high compressive strain in the *a*-*b* plane alters the quantum effects of the superlattice. We used ellipsometry to study the dielectric functions ($\varepsilon' + i\varepsilon''$) of the superlattice and a conventionally grown single crystal. The higher ε' of the superlattice indicates weakened quantum confinement by the compressed organic spacers (Fig. 3c), a larger Bohr radius in the multiple-quantum-well, and therefore a higher rate of free carrier generation (Supplementary Discussion 4)[14]. Besides, the shift in ε'', which reflects the absorption wavelength[27], suggests a smaller bandgap in the superlattice compared with the conventionally

grown single crystal, which is also evident by the longer-wavelength collection edge of the superlattice (Fig. 2f; Supplementary Fig. 16)[26]. Temperature-dependent photoluminescence measurements also show a much-reduced fitted exciton binding energy in the superlattice compared to the conventionally grown single crystal (Fig. 3d)[14,26]. In addition, the carrier lifetime in the superlattice is slightly longer than the conventionally grown single crystal at 0° in the transient photovoltage measurements (Fig. 1d)[26]. All these characteristics can be attributed to the weakened quantum confinement in the superlattice.

The enhanced carrier dynamics of the superlattice suggest potential improvements in photovoltaic performance. To relieve the compressive strain and create an even more stable structure, we investigated using Bi^{3+} (103 pm in radius[28]) to partially replace Sn^{2+} (118 pm in radius[29]). DFT calculations show that the Bi^{3+} tends to aggregate at the interface between the inorganic slab and the organic spacer to relieve the compressive strain (Fig. 4a, top; Supplementary Fig. 17), forming a Bi^{3+} rich atomic layer (Supplementary Fig. 18; Supplementary Discussion 5). This effectively decreases the formation energy of the superlattice and yields a much more stable structure (Supplementary Fig. 19). Furthermore, Bi^{3+} alloying alters the local electronic structure of the superlattice, which substantially decreases the conduction band minimum (CBM) (Fig. 4a, bottom; Supplementary Figs. 20 and 21)[30]. The region without Bi^{3+} alloying remains intact. The result is an inorganic slab with a double-band structure.

We grew 10% Bi^{3+}-alloyed $BA_2MA_4Sn_5I_{16}$ (n = 5) superlattices with a textured surface and fabricated solar cells directly on the substrate (Supplementary Figs. 22 and 23). We chose $BA_2MA_4Sn_5I_{16}$ due to its relatively weak quantum confinement, stable structure, and small bandgap. Indene-C60 bisadduct was used as the electron transport layer (ETL) because its CBM level (Supplementary Fig. 24) is higher than that of the Bi/Sn-I but lower than the Sn-I slabs (Supplementary Table 2). Because Bi^{3+} ions are distributed along the vertical slab direction, the Bi/Sn-I and the Sn-I regions are both in contact with the ETL. It is the first low-dimensional metal halide perovskite based solar cell to pass the quasi-steady state test (Supplementary Fig. 25). It exhibits a certified stable 12.36% photoelectric conversion efficiency—the highest in lead-free low-dimensional perovskite solar cells[19,31]. Moreover, the certified quantum efficiency plot of the solar cell (Fig. 4b; Supplementary Fig. 25) shows a carrier collection cutoff at ~1190 nm, which gives a bandgap of ~1.042 eV and a V_{OC} of at most 0.802 V according to Shockley-Queisser-limit[32,33]. However, the certified V_{OC} is 0.967 V, which is much higher than what detailed balance would allow.

Figure 4c shows the schematic band diagram of the solar cell. Because Bi^{3+} alloying in single-crystal perovskites will not lead to a high density of traps or band tail states, nor does it cause macroscale phase-separation between Bi^{3+} and Sn^{2+} regions (Supplementary Fig. 19)[34-36], the high V_{OC} is not attributed to any defect levels in the bandgap of the superlattice. The carrier collection cutoff of the solar cell is determined by the component of the lowest bandgap, i.e., 1.042 eV of the Bi/Sn-I region in this case. However, this low bandgap region does not seem

to affect the overall V_{OC} of the final device.

We performed wavelength-dependent *J-V* measurements of the solar cell to investigate the carrier transport process (Figs. 4d-4e). Under short incident wavelengths (< ~1000 nm), most electrons are excited into energy states higher than the CBM of both Sn-I and Bi/Sn-I regions. Those electrons from the Sn-I region naturally relax to the CBM of the Sn-I region. Additionally, a substantial portion of the electrons from the Bi/Sn-I region can also diffuse to the CBM of the Sn-I region through intra-band relaxation (solid blue arrows in Fig. 4c). This intra-band transition is possible because the ETL layer favors electron collection from the Sn-I region (solid red arrow in Fig. 4c). Moreover, the atomic-thin Bi/Sn-I region is easy for carriers to diffuse across. Therefore, most of carriers are in the Sn-I region, yielding a high V_{OC} and a high *F.F.* (Fig. 4d and 4e). Under long incident wavelengths (> ~1000 nm), electrons can only be excited in the Bi/Sn-I region. The relatively low-energy electrons cannot transit to the Sn-I region; they can only relax to the CBM of the Bi/Sn-I region, and then to the ETL via inter-band transition (dashed red arrows in Fig. 4c). Therefore, most of carriers are in the Bi/Sn-I region, yielding a low V_{OC} (Fig. 4d and 4e). The energy barrier between the Bi/Sn-I region and the ETL can cause serious charge accumulation and recombination (Supplementary Discussion 6)[37], which results in inefficient carrier transport and a low *F.F.* (Fig. 4d and 4e). When the device is excited under mixed incident wavelengths, the high-energy electrons excited in both Bi/Sn-I and Sn-I regions by the short wavelengths facilitate the quasi-fermi-level splitting in the Sn-I region. The low-energy electrons excited by the long wavelengths

234 will have a relatively small influence on the overall V_{OC}, because the long-wavelength portion
235 (between ~1000 nm and ~1200 nm) of the solar radiation spectrum is small (~9 %)[38,39], so the
236 quantity of the low-energy electrons is low. Therefore, the overall outcome is an unusually high
237 V_{OC} that is predominantly determined by the bandgap of the Sn-I region (Supplementary Fig
238 26, Supplementary Discussion 6).
239
240 Besides the unique intra-band relaxation mechanism discussed here, other carrier transport
241 processes may also be possible. More studies are needed to fully understand this intriguing
242 phenomenon. Further device performance improvements are possible with optimizations of the
243 design of the electrode patterns, the resistivity of the top electrode, and the band alignment of
244 the ETL/hole transport layer. The low-dimensional perovskites are intrinsically flexible without
245 any additional mechanical packaging because of the low bending stiffness of the inorganic
246 slabs (Supplementary Fig. 27)[40-43]. Therefore, these materials can be promising candidates for
247 large-area flexible solar cells as power sources for flexible devices that can be integrated with
248 non-planar surfaces. The strategy demonstrated here can be applied to general low-dimensional
249 perovskites, which may pave the way for exploring solution-based superlattice optoelectronics
250 with high efficiencies.
251
252 **METHODS**
253 **Materials.** The materials used in this study were as-purchased without further purification,
254 which included lead iodide (PbI_2, 99.99%, Tokyo Chemical Industry), lead bromide ($PbBr_2$

(98%, Alfa Aesar), hydrobromic acid (HBr, 48 wt% in water, Sigma Aldrich), methylamine (CH_3NH_2, 40% in methanol, Tokyo Chemical Industry), tin (II) oxide (SnO, 97%, Sigma Aldrich), hydroiodic acid (HI, 57% in water, Sigma Aldrich), hypophosphorous acid (H_3PO_2, 50 wt% in water, Sigma Aldrich), methylammonium iodide (MAI, 99.9%, Greatcell Solar), n-butylammonium iodide (BAI, 99.9%, Greatcell Solar), cesium chloride (CsCl, 99.9%, Sigma Aldrich), silver chloride (AgCl, 99%, Sigma Aldrich), antimony (III) chloride ($SbCl_3$, 99%, Sigma Aldrich), bismuth (III) iodide (BiI_3, 99%, Sigma Aldrich), indene-C60 Bisadduct (ICBA, LT-S9030, Luminescence Technology), poly[bis(4-phenyl)(2,4,6-trimethylphenyl)amine] (PTAA, LT-N168, Luminescence Technology), chlorobenzene (C_6H_5Cl, TCI America), anhydrous dimethylformamide (DMF, C_3H_7NO, 99.8%, Sigma Aldrich), anhydrous gamma-butyrolactone (GBL, $C_4H_6O_2$, 99% Sigma Aldrich), anhydrous dimethyl sulfoxide (DMSO, C_2H_6OS, 99.9%, Sigma Aldrich), isopropanol (IPA, C_3H_8O, 99.5%, Sigma Aldrich), and methanol (99.8%, CH_3OH, Sigma Aldrich).

Preparation of single-crystal perovskites. $MAPbBr_3$: Flat and smooth centimeter-sized bulk $MAPbBr_3$ single crystals were prepared by solution-based growth[20]. The $MAPbBr_3$ were used as the 3D perovskite substrate to grow the low-dimensional perovskite superlattice without any further treatment. $MAPbI_3$: $MAPbI_3$ single crystals were prepared by solution-based growth[22]. The as-obtained crystals were ultrasonically cleaned in an anhydrous IPA solvent for 5 mins. Then, the crystals were crushed into powers for growth precursor preparation.

Synthesis of low-dimensional perovskites. 0.3 g SnO powder was dissolved into a mixture of 3 ml hydroiodic acid solution and 0.5 ml hypophosphorous acid solution in a glass vial by heating to 180 °C under constant stirring until a bright yellow precursor solution was obtained. BA_2SnI_4 crystals were synthesized by injecting 1 mL BAI solution (2.5 mmol BAI in 1 mL methanol) into the precursor solution. $BA_2MA_2Sn_3I_{10}$ crystals were synthesized by injecting 1 mL MAI/BAI solution (1.67 mmol MAI and 0.83 mmol BAI in 1 mL methanol) into the precursor solution. $BA_2MA_4Sn_5I_{16}$ crystals were synthesized by injecting 1 mL MAI/BAI solution (2 mmol MAI and 0.5 mmol BAI in 1 mL methanol) into the precursor solution. Then, the vial was transferred into a nitrogen-filled glove box at room temperature. The as-formed crystals were then isolated by removing the solution, then quickly washed using IPA for three times. Then, the crystals were dried and then directly dissolved in GBL to form the growth solution (0.5 M) for low-dimensional perovskites. For the Bi^{3+} alloyed superlattice, 10% molar ratio of BiI_3 was also dissolved into the growth solution.

Preparation of precursors for mixed perovskites and double perovskites. The $MAPb_{0.5}Sn_{0.5}Br_3$ was prepared by mixing MABr, $PbBr_2$, and $SnBr_2$ with a 2:1:1 molar ratio in DMF (1.5 M). The double perovskites $Cs_2AgSbCl_6$ precursor solution was prepared by directly mixing CsCl, AgCl, and $SbCl_3$ with a 2:1:1 molar ratio in DMSO (0.4 M). The as-prepared solution was stirred under 60 °C until the solution became clear. Then, 0.4 M $MAPbI_3$ single crystal power is added to the solution to complete precursor solution preparation for achieving a suitable lattice constant with minimal lattice mismatch between the substrate and the

297 inorganic slab of the epitaxial layer.

298

299 **Device fabrication.** $MAPbBr_3$ bulk crystals were used as the three-dimensional (3D) substrates
300 as their synthesis is well-established. To further reduce the lattice mismatch, the mixed
301 perovskite (or double perovskite) precursor was casted onto the $MAPbBr_3$ layer while hot to
302 form a smooth epitaxial layer, which was the actual surface for growing the low-dimensional
303 perovskites. The thickness of the smooth epitaxial layer does not influence the subsequent
304 superlattice growth or device fabrication. Polyimide films (12.7 μm thick) were pre-patterned
305 (with an opening size of 1 μm by 1 μm) to serve as the growth mask by following a reported
306 method[22]. Then, a layer of Au was deposited by sputtering to serve as the bottom electrode.
307 Later, the PTAA solution (1.5 mg/mL in anhydrous toluene) was directly spin-coated onto the
308 patterned polyimide/Au films at 2500 rpm for 30 s, followed by annealing at 80 °C for 3 min.
309 Then the growth substrate was laminated with the polyimide/Au/PTAA mask and then spin-
310 coated by supersaturated mixed perovskite (or double perovskite) precursor at 4000 rpm for 30
311 s followed by annealing at 100 °C for 5 min. Subsequently, low-dimensional perovskite growth
312 solution (0.5 M in GBL) was spin-coated on the substrate at 1500 rpm for 60 s followed by
313 annealing at 180 °C for 2 min to form the superlattice absorber layer. After that, ICBA (20
314 mg/mL in chlorobenzene) was spin-coated onto the epitaxial layer, followed by annealing at
315 100 °C for 5 min. Finally, a layer of ITO was deposited by sputtering to serve as the transparent
316 top electrode.

317

DFT calculations. First-principles DFT calculations were performed using the Vienna *Ab initio* Simulation Package[44]. The Projector Augmented Wave pseudopotential was used for describing electron-ion interactions[45]. The Generalized Gradient Approximation parametrized by Perdew, Burke, and Ernzerhof was used to treat the electron-electron exchange-correlation functional[46]. The van der Waals functional DFT-D3 was applied to properly describe the long-range dispersion interactions between the organic molecules in the hybrid materials[47]. The hybrid functionals within Heyd-Scuseria-Ernzerhof formalism with 70% Hartree-Fock exchange were employed to calculate band gaps for the Sn-based perovskites[48,49]. The wave functions were expanded in a plane-wave basis set with a cutoff energy of 400 eV. The structures for conventionally grown single crystal Ruddlesden-Popper perovskites and epitaxially grown perovskites were built based on experimental results of the lattices. The atomic positions were fully optimized until all components of the residual forces were smaller than 0.03 eV/Å. The convergence threshold for self-consistent-field iteration was set at 10^{-5} eV. Γ-centered 2×1×4 and 4×4×1 k-point grids were used for superlattice and conventionally grown single crystals, respectively. Due to the limited computational resources, we could only simulate the $n = 3$ structure, but this will not influence the device ($n = 5$) because the formation mechanism of the double-bandgap structure is the same.

Morphology characterization. All scanning electron microscope (SEM) images were taken using a Zeiss Sigma 500 SEM. All optical images were taken using a Zeiss Axio Imager Optical Microscope.

Structure characterization. X-ray diffraction was measured by a Rigaku 393 Smart lab diffractometer equipped with a Cu Kα1 radiation source (λ = 0.15406 nm) and a Ge 394 (220 × 2) monochromator. The scanning transmission electron microscopy (STEM) images were taken using a cryo-FEI 200 kV Sphera microscope. Samples for the STEM were prepared using a frozen focused ion beam (FEI Scios Dual Beam FIB/SEM). The conventionally grown single crystal was hard to be imaged by STEM since the sample without an epitaxial substrate curled quickly due to its instability in the STEM. X-ray photoelectron spectroscopy (XPS) measurements were carried out using Kratos AXIS Supra with a He I (21.22 eV) source under 10^{-8} torr chamber pressure.

Optical characterizations. Photoluminescence (PL) and time-resolved PL (TRPL) measurements were performed with a confocal microscope system focusing a monochromatic 6 ps-pulsed laser with a ×4 objective lens (numerical aperture 0.13). Optical functions were measured by ellipsometry (J.A. Woollam M-2000D Spectroscopic Ellipsometer). Ultraviolet photoelectron spectroscopy (UPS) measurements were carried out using Kratos AXIS Supra with a He I (21.22 eV) source under 10^{-8} torr chamber pressure. Ultraviolet-visible spectroscopy (UV-vis) and absorption spectra were collected using a Perkin Elmer Lambda 1050 UV-vis system under the reflection mode.

Electrical characterizations. Polarized photocurrent was measured with a polarizer. Time-of-

flight was measured by extracting the decay time of the transient photocurrent to calculate the carrier mobility. An external bias of 0.5 V was used to power the devices with a resistor connected in series. Orientation-dependent transient photovoltages were measured with an oscilloscope (Agilent MSO6104A Channel Mixed Signal) to study the carrier lifetime. A pulsed laser with a pulse width of less than 10^{-10} s was used as the light source. The electron beam induced photocurrent (EBIC) was collected using a FEI Scios Dual Beam microscope with a Mighty EBIC 2.0 controller (Ephemeron Labs) and a Femto DLPCA-200 preamplifier. Lateral Au electrodes were deposited by electron-beam evaporation for surface measurements; a pre-patterned Au-coated polyimide film was used as the bottom electrode for cross-section measurements; the top surface was deposited with a layer of Au by electron-beam evaporation to serve as the top electrode. The EBIC and SEM images of the same region of interest were collected simultaneously. The samples were several micrometers in thickness, while EBIC could penetrate up to several micrometers into the samples[50].

Photovoltaic characterizations. Current density-voltage (*J-V*) measurements were carried out using a Keithley 2400 source meter under a simulated air mass of 1.5 irradiation (100 mW/cm^2) and a xenon-lamp-based solar simulator (Oriel LCS-100). Temperature-dependent *J-V* measurements were performed with the sample in a liquid nitrogen cooled metal tank, where one side was glass to allow illumination. The same configuration was used for both epitaxial and polycrystalline devices. External quantum efficiency (EQE) data were collected by illuminating the device under monochromatic light using a tungsten source (chopped at 150

Hz) while collecting the photocurrent by a lock-in amplifier in the alternating current mode. The 2D mapping of the thickness-dependent EQE was generated from the Contour-Color Fill function. Wavelength-dependent *J-V* measurements were carried out by applying a series of bandpass filters (Newport) under the solar simulator to measure both the polycrystalline and epitaxial devices.

FIGURE CAPTIONS

Fig. 1 | Structural characterizations of the BA_2SnI_4 superlattice. (**a**) Scanning electron microscope images showing the crisscross epitaxial BA_2SnI_4 superlattice before and after merging into a thin film. (**b**) Schematics and atomic-resolution cryogenic-scanning transmission electron microscopy images showing the superlattice structure of a single plate. Cryogenic-scanning transmission electron microscope is essential to minimize the damage of beam-sensitive materials. The epitaxial layer has a well-aligned anisotropic structure without grain boundaries or dislocations. The insets are fast Fourier transform (FFT) patterns from the epitaxial layer in the *a-c* plane, which show a two-dimensional diffraction pattern of the superlattice and is different from that of the substrate. The inset FFT images in the *b-c* plane show the structural similarity between the inorganic slab and the substrate. Organic atoms are usually invisible under electron diffraction. (**c**) Photocurrent measurements with a linearly polarized excitation source showing that the response of the epitaxial layer (top) exhibits a period that is half of a conventionally grown single crystal (bottom). (**d**) Transient photovoltage measurements showing the orientation-dependent carrier lifetime in the *a-b* plane. The inset

optical image shows the measurement setup. The error bars are from measurements of five different devices.

Fig. 2 | Carrier transport properties of the BA_2SnI_4 superlattice. (**a**) Transient photocurrent measurements along the film thickness (*c*) direction. The superlattice shows the highest carrier mobility. The carrier mobility in the polycrystal is limited by grain boundaries and lattice misalignments between grains. The conventionally grown single crystal shows the lowest carrier mobility because of the energy barriers caused by the organic spacers along the film thickness direction. The inset shows the schematic measurement setup. The error bars are from measurements of five different devices. (**b**) Time-resolved photoluminescence measurements showing a longer carrier lifetime in the superlattice than the polycrystal. The lifetime-power relationship in the polycrystal tends to deviate from a linear fit (the dashed lines) at high excitation power due to absorber degradation. The error bars are from measurements of five different devices. (**c**) Temperature-dependent *J-V* measurements on solar cells (ITO/ICBA/perovskite/PTAA/Au; active size, 1 mm^2) fabricated on as-grown films. The current density values are normalized. As temperature drops, the *F.F.* of the superlattice device does not change as dramatically as the polycrystal device, indicating a lower internal energy barrier in the superlattice. (**d**) Scanning electron microscope images and corresponding EBIC mapping of the top surface of BA_2SnI_4 films. The polycrystal exhibits grain-dependent current signals. The superlattice exhibits stronger current signals with a crisscross pattern even with a smooth film surface. (**e**) Scanning electron microscopy images and corresponding EBIC

mapping of the cross-section of BA_2SnI_4 films. The polycrystal exhibits grain-dependent current signals. The superlattice exhibits stronger current signals with a linear pattern. (**f**) Thickness-dependent EQE measurements. The superlattice device exhibits a higher EQE with a larger optimum absorber thickness, indicating the carrier diffusion length in the superlattice is longer than that in the polycrystal. A broader collection range also indicates a smaller bandgap in the superlattice.

Fig. 3 | Strain properties of $BA_2MA_{n-1}Sn_nI_{3n+1}$ superlattices. (**a**) X-ray diffraction measurements of the BA_2SnI_4 superlattice and conventionally grown BA_2SnI_4 single crystals. A compressive strain in the *a*-*b* plane and a tensile strain along the *c* direction are observed in the superlattice. (**b**) DFT computed and experimentally calculated lattice strain with different *n* in low-dimensional $BA_2MA_{n-1}Sn_nI_{3n+1}$ perovskites. Crystals with larger *n* will have smaller strain. Inset scanning electron microscope images show that a larger *n* will result in a smoother surface, which is attributed to less defects under smaller epitaxial strain. (**c**) Ellipsometry measurements of the dielectric function ($\varepsilon' + i\varepsilon''$) of the $BA_2MA_2Sn_3I_{10}$ superlattice and conventionally grown $BA_2MA_2Sn_3I_{10}$ single crystals. The larger ε' in the superlattice indicates that the compressive strain can increase the dielectric constant and the Bohr radius in the superlattice. A redshift in the ε'' reveals that the compressive strain decreases the bandgap of the superlattice. (**d**) Estimated exciton binding energies obtained from temperature-dependent photoluminescence measurements. The smaller fitted exciton binding energy in the superlattice than the polycrystal indicates a weaker quantum confinement effect because of the

smaller width of the organic barrier. In the inset equation, I is the integrated photoluminescent intensity, I_0 is the integrated intensity at room temperature, A is an arbitrary constant, E_B is the exciton binding energy, k_B is the Boltzmann constant, and T is the temperature.

Fig. 4 | Photovoltaic studies of Bi^{3+}-alloyed $BA_2MA_2Sn_3I_{10}$ superlattice. (**a**) Structure of the Bi^{3+}-alloyed $BA_2MA_2Sn_3I_{10}$ superlattice computed by DFT. The Bi^{3+} ions preferentially aggregate at the interface between the organic and inorganic slabs to relieve the lattice strain (top). The Bi^{3+} alloying alters the electronic band structure, resulting in a substantially decreased CBM. Combined with the region without Bi^{3+}, they form a double-band structure in the inorganic slab (bottom). (**b**) Certified photovoltaic performance measurement, showing a bandgap of 1.042 eV and a V_{OC} of 0.967 V, beyond the Shockley-Queisser-limit. (**c**) Unusual carrier transport processes with intra-band relaxation, resulting in beyond-band quasi-fermi-level splitting, and therefore, the high V_{OC}. Note that both Sn-I and Bi/Sn-I regions are in direct physical contact with the ETL. (**d**) Single-wavelength excited *J-V* measurements of a polycrystalline solar cell with a uniform Bi^{3+} distribution and therefore, a single bandgap (left) and a superlattice (right) solar cell. In the polycrystalline device, reasonably small variations in the *F.F.* and V_{OC} are observed, indicating that the carrier transport and the collection efficiency are almost wavelength-independent. In the superlattice device, when the incident wavelength is shorter than ~900 nm, neither *F.F.* nor V_{OC} exhibits an obvious wavelength-dependency. However, once the excitation wavelength is longer than ~900 nm, both *F.F.* and V_{OC} drop substantially. (**e**) Extracted *F.F.* and V_{OC} from (**d**).

REFERENCES

1 Zhang, W. et al. Metal halide perovskites for energy applications. *Nat. Energy* **1**, 1-8 (2016).

2 de Arquer, F. P. G. et al. Solution-processed semiconductors for next-generation photodetectors. *Nat. Rev. Mater.* **2**, 1-17 (2017).

3 Lei, Y. et al. Single-crystal halide perovskites: Opportunities and challenges. *Matter* **4**, 2266-2308 (2021).

4 Meng, L. et al. Addressing the stability issue of perovskite solar cells for commercial applications. *Nat. Commun.* **9**, 1-4 (2018).

5 Park, N. G. Research direction toward scalable, stable, and high efficiency perovskite solar cells. *Adv. Energy Mater.* **10**, 1903106 (2020).

6 Ke, W. et al. Prospects for low-toxicity lead-free perovskite solar cells. *Nat. Commun.* **10**, 965 (2019).

7 Tsai, H. et al. High-efficiency two-dimensional Ruddlesden–Popper perovskite solar cells. *Nature* **536**, 312-316 (2016).

8 Blancon, J.-C. et al. Extremely efficient internal exciton dissociation through edge states in layered 2D perovskites. *Science* **355**, 1288-1292 (2017).

9 Yang, X. et al. Efficient green light-emitting diodes based on quasi-two-dimensional composition and phase engineered perovskite with surface passivation. *Nat. Commun.* **9**, 1-8 (2018).

10 Qin, C. et al. Stable room-temperature continuous-wave lasing in quasi-2D perovskite films. *Nature* **585**, 53-57 (2020).

11 Kumar, A. et al. Excitons in 2D perovskites for ultrafast terahertz photonic devices. *Sci. Adv.* **6**, eaax8821 (2020).

12 Chen, A. Z. et al. Origin of vertical orientation in two-dimensional metal halide perovskites and its effect on photovoltaic performance. *Nat. Commun.* **9**, 1-7 (2018).

13 Fang, H.-H. et al. Long-lived hot-carrier light emission and large blue shift in formamidinium tin triiodide perovskites. *Nat. Commun.* **9**, 1-8 (2018).

14 Cheng, B. et al. Extremely reduced dielectric confinement in two-dimensional hybrid perovskites with large polar organics. *Commun. Phys.* **1**, 1-8 (2018).

15 Soe, C. M. M. et al. Structural and thermodynamic limits of layer thickness in 2D halide perovskites. *Proc. Natl. Acad. Sci.* **116**, 58-66 (2019).

16 Blancon, J.-C. et al. Scaling law for excitons in 2D perovskite quantum wells. *Nat. Commun.* **9**, 1-10 (2018).

17 Gélvez-Rueda, M. C. et al. Overcoming the exciton binding energy in two-dimensional perovskite nanoplatelets by attachment of conjugated organic chromophores. *Nat. Commun.* **11**, 1-9 (2020).

18 Grancini, G. et al. Dimensional tailoring of hybrid perovskites for photovoltaics. *Nat. Rev. Mater.* **4**, 4-22 (2019).

19 Ke, W. et al. Prospects for low-toxicity lead-free perovskite solar cells. *Nat. Commun.* **10**, 1-4 (2019).
20 Lei, Y. et al. Controlled Homoepitaxial Growth of Hybrid Perovskites. *Adv. Mater.* **30**, 1705992 (2018).
21 Chen, Y. et al. Strain engineering and epitaxial stabilization of halide perovskites. *Nature* **577**, 209-215 (2020).
22 Lei, Y. et al. A fabrication process for flexible single-crystal perovskite devices. *Nature* **583**, 790-795 (2020).
23 Rothmann, M. U. et al. Atomic-scale microstructure of metal halide perovskite. *Science* **370** (2020).
24 Tsai, H. et al. Light-induced lattice expansion leads to high-efficiency perovskite solar cells. *Science* **360**, 67-70 (2018).
25 Tsai, H. et al. Design principles for electronic charge transport in solution-processed vertically stacked 2D perovskite quantum wells. *Nat. Commun.* **9**, 1-9 (2018).
26 Liu, S. et al. Manipulating efficient light emission in two-dimensional perovskite crystals by pressure-induced anisotropic deformation. *Sci. Adv.* **5**, eaav9445 (2019).
27 Fujiwara, H. *Spectroscopic ellipsometry: principles and applications*. (John Wiley & Sons, 2007).
28 Chatterjee, S. et al. Influence of metal substitution on hybrid halide perovskites: towards lead-free perovskite solar cells. *J. Mater. Chem. A* **6**, 3793-3823 (2018).
29 Abdel-Shakour, M. et al. High‐Efficiency Tin Halide Perovskite Solar Cells: The Chemistry of Tin (II) Compounds and Their Interaction with Lewis Base Additives during Perovskite Film Formation. *Sol. RRL* **5**, 2000606 (2021).
30 Hasegawa, H. et al. Effective band gap tuning by foreign metal doping in hybrid tin iodide perovskites. *J. Mater. Chem. C* **5**, 4048-4052 (2017).
31 Liao, Y. et al. Highly oriented low-dimensional tin halide perovskites with enhanced stability and photovoltaic performance. *J. Am. Chem. Soc.* **139**, 6693-6699 (2017).
32 Ruppel, W. et al. Upper limit for the conversion of solar energy. *IEEE Trans. Electron Devices* **27**, 877-882 (1980).
33 De Vos, A. et al. On the thermodynamic limit of photovoltaic energy conversion. *Appl. Phys.* **25**, 119-125 (1981).
34 Li, C. et al. Highly conductive n-type CH 3 NH 3 PbI 3 single crystals doped with bismuth donors. *J. Mater. Chem. C* **8**, 3694-3704 (2020).
35 Bartolomé, J. et al. Huge Photostability Enhancement in Bismuth-Doped Methylammonium Lead Iodide Hybrid Perovskites by Light-Induced Transformation. *Chem. Mater.* **31**, 3662-3671 (2019).
36 Kang, Y. et al. Influence of Bi doping on physical properties of lead halide perovskites: a comparative first-principles study between CsPbI3 and CsPbBr3. *Mater. Today Adv.* **3**, 100019 (2019).
37 He, T. et al. Reduced-dimensional perovskite photovoltaics with homogeneous energy landscape. *Nat. Commun.* **11**, 1-11 (2020).
38 Huang, X. et al. Enhancing solar cell efficiency: the search for luminescent materials

as spectral converters. *Chem. Soc. Rev.* **42**, 173-201 (2013).
39 Kruse, O. et al. Photosynthesis: a blueprint for solar energy capture and biohydrogen production technologies. *Photochem. Photobiol. Sci.* **4**, 957-970 (2005).
40 Quan, L. N. et al. Ligand-stabilized reduced-dimensionality perovskites. *J. Am. Chem. Soc.* **138**, 2649-2655 (2016).
41 Spanopoulos, I. et al. Uniaxial expansion of the 2D Ruddlesden–Popper perovskite family for improved environmental stability. *J. Am. Chem. Soc.* **141**, 5518-5534 (2019).
42 Smith, I. C. et al. A layered hybrid perovskite solar‐cell absorber with enhanced moisture stability. *Angew. Chem.* **126**, 11414-11417 (2014).
43 Stoumpos, C. C. et al. Ruddlesden–Popper hybrid lead iodide perovskite 2D homologous semiconductors. *Chem. Mater.* **28**, 2852-2867 (2016).
44 Kresse, G. et al. Efficient iterative schemes for ab initio total-energy calculations using a plane-wave basis set. *Phys. Rev. B* **54**, 11169 (1996).
45 Blöchl, P. E. Projector augmented-wave method. *Phys. Rev. B* **50**, 17953 (1994).
46 Perdew, J. P. et al. Generalized gradient approximation made simple. *Phys. Rev. Lett.* **77**, 3865 (1996).
47 Grimme, S. et al. A consistent and accurate ab initio parametrization of density functional dispersion correction (DFT-D) for the 94 elements H-Pu. *J. Chem. Phys.* **132**, 154104 (2010).
48 Heyd, J. et al. Hybrid functionals based on a screened Coulomb potential. *J. Chem. Phys.* **118**, 8207-8215 (2003).
49 Yang, D. et al. Functionality-directed screening of Pb-free hybrid organic–inorganic perovskites with desired intrinsic photovoltaic functionalities. *Chem. Mater.* **29**, 524-538 (2017).
50 Powell, K. M. et al. Depth-dependent EBIC microscopy of radial-junction Si micropillar arrays. *Appl. Microsc.* **50**, 1-9 (2020).

Acknowledgements We thank S. Xiang for constructive feedback on preparing the manuscript and D. Fenning for inspiring discussions on the data analysis. **Funding:** This work was supported by a Sloan Research Fellowship from the Alfred P. Sloan Foundation and a Lattimer Faculty Research Fellowship from the University of California San Diego. The microfabrication involved in this work was performed at the San Diego Nanotechnology Infrastructure (SDNI) of UCSD, a member of the National Nanotechnology Coordinated Infrastructure, which was supported by the National Science Foundation (Grant No. ECCS-

1542148); This work was performed, in part, at the Center for Integrated Nanotechnologies, an Office of Science User Facility operated for the U.S. Department of Energy (DOE) Office of Science at Los Alamos National Laboratory, Stanford Nano Shared Facilities (SNSF, supported by the National Science Foundation under award ECCS-1542152), and Stanford Synchrotron Radiation Laboratory (SSRL, a national user facility operated by Stanford University on behalf of the U.S. Department of Energy, Office of Basic Energy Sciences). The computational work used the Extreme Science and Engineering Discovery Environment (XSEDE), which is supported by the National Science Foundation grant number OCI-1053575.

Author contributions S.X. and Y.Lei conceived the idea. Y.Li carried out the DFT calculations. Y.Lei and C.C.F.L. synthesized the materials, prepared the substrates, and fabricated the devices. Y.Lei, Q.Y., S.Z., H.G., and Y.C. contributed to the structural characterizations. J.Z. contributed to the optical and electrical characterizations. R.Z. carried out the FTIR characterizations and the simulations. All authors contributed to analyzing the data and commenting on the manuscript. **Competing interests:** The authors declare no competing interests. **Data and materials availability:** All data are available in the manuscript or supplementary materials.

Figures

Figure 1

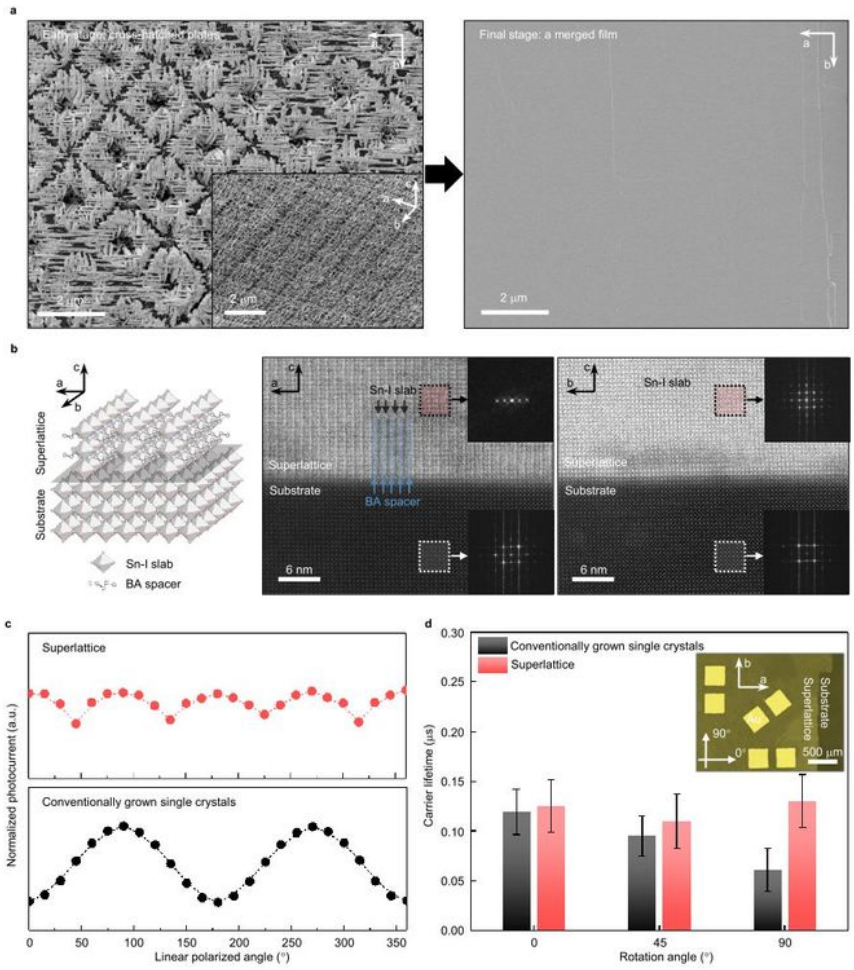

Figure 1

Structural characterizations of the BA2SnI4 superlattice. (a) Scanning electron microscope images showing the crisscross epitaxial BA2SnI4 superlattice before and after merging into a thin film. (b) Schematics and atomic-resolution cryogenic-scanning transmission electron microscopy images

showing the superlattice structure of a single plate. Cryogenic-scanning transmission electron microscope is essential to minimize the damage of beam-sensitive materials. The epitaxial layer has a well-aligned anisotropic structure withoutgrain boundaries or dislocations. The insets are fast Fourier transform (FFT) patterns from theepitaxial layer in the a-c plane, which show a two-dimensional diffraction pattern of the superlattice and is different from that of the substrate. The inset FFT images in the b-c plane show the structural similarity between the inorganic slab and the substrate. Organic atoms are usually invisible under electron diffraction. (c) Photocurrent measurements with a linearly polarized excitation source showing that the response of the epitaxial layer (top) exhibits a period that is half of a conventionally grown single crystal (bottom). (d) Transient photovoltage measurements showing the orientation-dependent carrier lifetime in the a-b plane. The inset 20 optical image shows the measurement setup. The error bars are from measurements of five different devices.

Figure 2

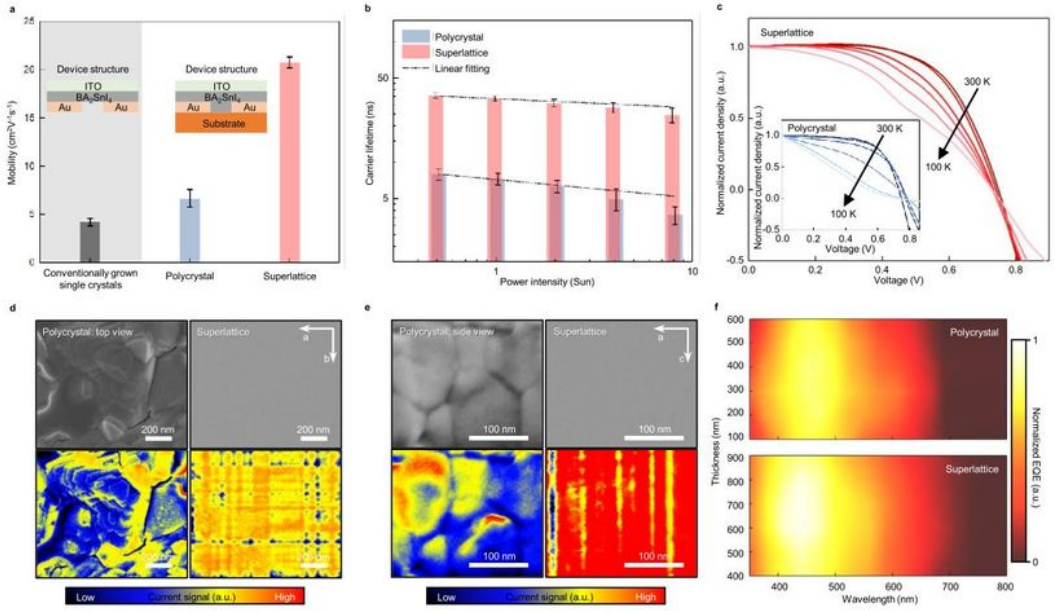

Figure 2

Carrier transport properties of the BA2SnI4 superlattice. (a) Transient photocurrent measurements along the film thickness (c) direction. The superlattice shows the highest carrier mobility. The carrier mobility in the polycrystal is limited by grain boundaries and lattice misalignments between grains. The conventionally grown single crystal shows the lowestcarrier mobility because of the energy barriers caused by the organic spacers along the film thickness direction. The inset shows the schematic

measurement setup. The error bars are from measurements of five different devices. (b) Time-resolved photoluminescence measurements showing a longer carrier lifetime in the superlattice than the polycrystal. The lifetime-power relationship in the polycrystal tends to deviate from a linear fit (the dashed lines) at high excitation power due to absorber degradation. The error bars are from measurements of five different devices. (c) Temperature-dependent J-V measurements on solar cells (ITO/ICBA/perovskite/PTAA/Au; active size, 1 mm2) fabricated on as-grown films. The current density values are normalized. As temperature drops, the F.F. of the superlattice devicedoes not change as dramatically as the polycrystal device, indicating a lower internal energy barrier in the superlattice. (d) Scanning electron microscope images and corresponding EBIC mapping of the top surface of BA2SnI4 films. The polycrystal exhibits grain-dependent current signals. The superlattice exhibits stronger current signals with a crisscross pattern even with a smooth film surface. (e) Scanning electron microscopy images and corresponding EBIC 21 mapping of the cross-section of BA2SnI4 films. The polycrystal exhibits grain-dependent current signals. The superlattice exhibits stronger current signals with a linear pattern. (f) Thickness-dependent EQE measurements. The superlattice device exhibits a higher EQE with a larger optimum absorber thickness, indicating the carrier diffusion length in the superlattice is longer than that in the polycrystal. A broader collection range also indicates a smaller bandgap in the superlattice.

Figure 3

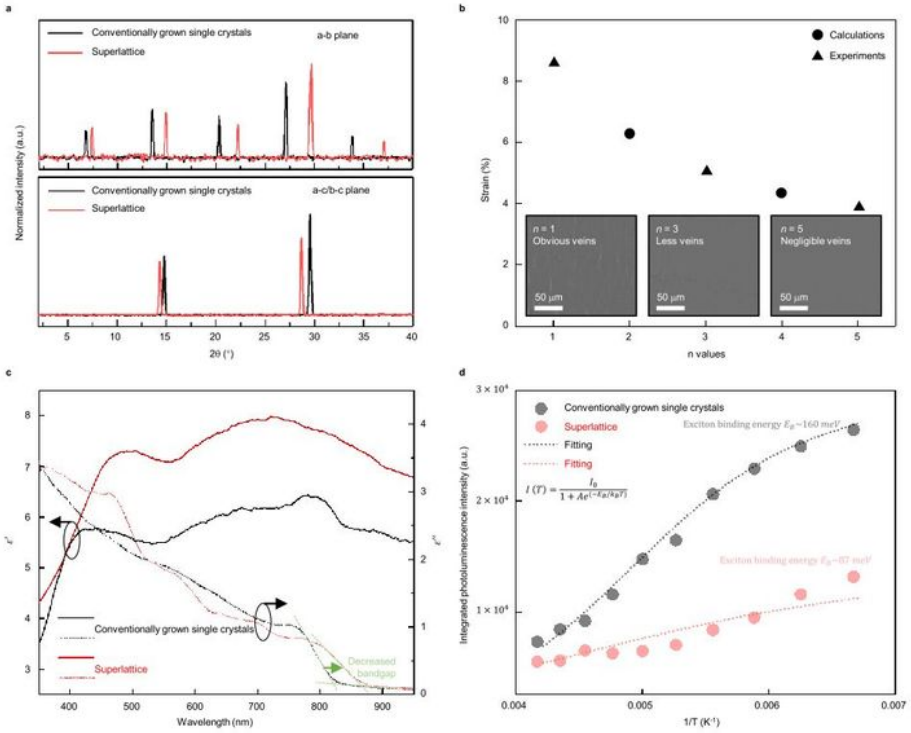

Figure 3

Strain properties of BA2MAn−1SnnI3n+1 superlattices. (a) X-ray diffraction measurements of the BA2SnI4 superlattice and conventionally grown BA2SnI4 single crystals. A compressive strain in the a-b plane and a tensile strain along the c direction are observed in the superlattice. (b) DFT computed and experimentally calculated lattice strain with different n in low-dimensional BA2MAn−1SnnI3n+1 perovskites. Crystals with larger n will have smaller strain. Inset scanning electron microscope images

show that a larger n will result in a smoother surface, which is attributed to less defects under smaller epitaxial strain. (c) Ellipsometry measurements of the dielectric function (ε ' + ε ") of the BA2MA2Sn3I10 superlattice and conventionally grown BA2MA2Sn3I10 single crystals. The larger ε' ' in the superlattice indicates that the compressive strain can increase the dielectric constant and the Bohr radius in the superlattice. A redshift in the ε" " reveals that the compressive strain decreases the bandgap of the superlattice. (d) Estimated exciton binding energies obtained from temperature dependent photoluminescence measurements. The smaller fitted exciton binding energy in the superlattice than the polycrystal indicates a weaker quantum confinement effect because of the 22 smaller width of the organic barrier. In the inset equation, I is the integrated photoluminescent intensity, I0 is the integrated intensity at room temperature, A is an arbitrary constant, Eb is the exciton binding energy, kB is the Boltzmann constant, and T is the temperature.

Figure 4

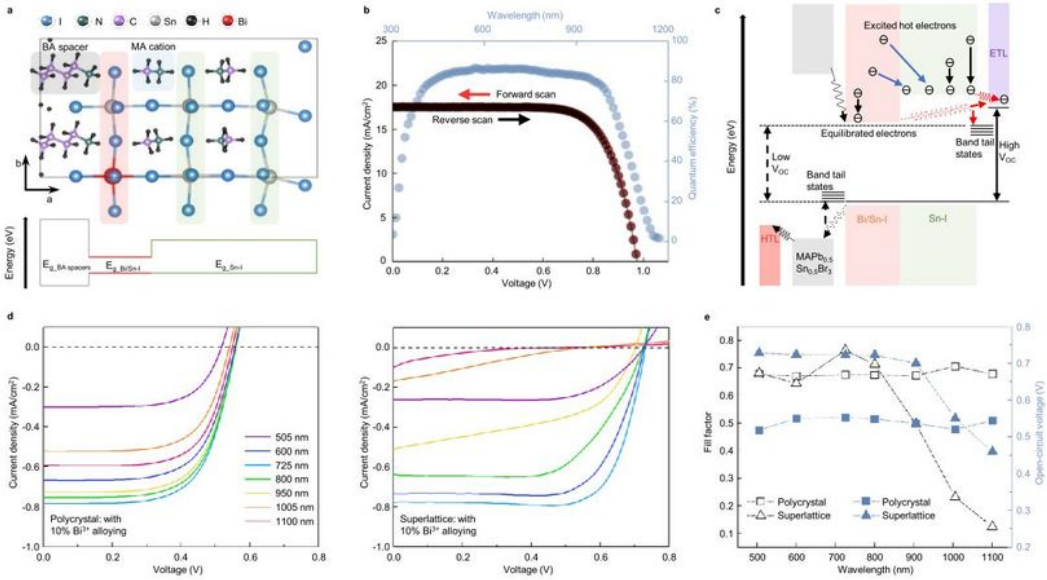

Figure 4

Photovoltaic studies of Bi3+ -alloyed BA2MA2Sn3I10 superlattice. (a) Structure of the Bi3+-alloyed BA2MA2Sn3I10 superlattice computed by DFT. The Bi3+ ions preferentially aggregate at the interface between the organic and inorganic slabs to relieve the lattice strain (top). The Bi3+ alloying alters the electronic band structure, resulting in a substantially decreased CBM. Combined with the region without Bi3+ , they form a double-band structure in the inorganic slab (bottom). (b) Certified photovoltaic

performance measurement, showing a bandgap of 1.042 eV and a VOC of 0.967 V, beyond the Shockley-Queisser-limit. (c) Unusual carrier transport processes with intra-band relaxation, resulting in beyond-band quasi-fermi level splitting, and therefore, the high VOC. Note that both Sn-I and Bi/Sn-I regions are in direct physical contact with the ETL. (d) Single-wavelength excited J-V measurements of a polycrystalline solar cell with a uniform Bi3+ distribution and therefore, a single bandgap (left) and a superlattice (right) solar cell. In the polycrystalline device, reasonably small variations in the F.F. and VOC are observed, indicating that the carrier transport and the collection efficiency are almost wavelength-independent. In the superlattice device, when the incident wavelength is shorter than ~900 nm, neither F.F. nor VOC exhibits an obvious wavelength dependency. However, once the excitation wavelength is longer than ~900 nm, both F.F. and VOC drop substantially. (e) Extracted F.F. and VOC from (d).

Supplementary Files

This is a list of supplementary files associated with this preprint. Click to download.

- Leisupplement.pdf